Attenuation correction for the HRRT PET-scanner using transmission scatter correction and total variation regularization

Sune H. Keller, Claus Svarer and Merence Sibomana

***Abstract*— In the standard software for the Siemens high resolution research tomograph (HRRT) positron emission tomography (PET) scanner the most commonly used segmentation in the μ-map reconstruction for human brain scans is maximum a posteriori for transmission (MAP-TR). Bias in the lower cerebellum and pons in HRRT brain images have been reported. The two main sources of the problem with MAP-TR are poor bone / soft tissue segmentation below the brain and overestimation of bone mass in the skull.**

Method: We developed the new transmission processing with total variation (TXTV) method that introduces scatter correction in the μ-map reconstruction and total variation filtering to the transmission processing.

Results: Comparing MAP-TR and the new TXTV with gold standard CT-based attenuation correction, we found that TXTV has less bias as compared to MAP-TR. We also compared images acquired at the HRRT scanner using TXTV to the GE Advance scanner images and found high quantitative correspondence. TXTV has been used to reconstruct more than 4000 HRRT scans at 7 different sites with no reports of biases.

Conclusion: TXTV-based reconstruction is recommended for human brain scans on the HRRT.

***Index Terms*— HRRT, attenuation correction, transmission scatter correction, PET, total variation**

I. Introduction

THE high resolution research tomograph (HRRT, CTI/Siemens) is a positron emission tomography (PET) scanner dedicated to human brain scanning [1], [2], [3]. It has resolution of 1.4 mm using point spread function modeling (PSF) [4], which is 2-3 times better than other human PET scanners (typically PET/CT) [5] (see Fig. 1A-B). This high resolution makes it ideal for neurology studies.

In the image reconstruction of PET emission scans (EM) one has to do attenuation correction (AC) to account for the PET signal loss in matter using a so-called μ-map. Today most PET scanners in use are PET/CTs, and the μ-map is derived from CT scans by a mapping from the CT-energy range to the 511 keV of the photons detected in PET. For PET scanners without a CT such as the HRRT, a transmission scan (TX) is performed by rotating a radioactive transmission source with an energy of, or close to, 511keV around the object in the scanner and from that a μ-map for attenuation correction is created.

The HRRT scanner software offers 3 choices for transmission scan processing (image reconstruction and possible post processing) of which maximum a posteriori for transmission (MAP-TR) [6], [7], [8] is most widely used. MAP-TR was shown by van Velden et al. [9] to provide the most accurate μ-maps for human brains amongst the methods available for the HRRT, but the paper also showed MAP-TR to have shortcomings as it was also the case with the works by Anton-Rodriguez et al. [10] and Son et al. [11]. The major issues with MAP-TR are overestimation of the skull attenuation, inaccurate segmentation of bone structures at the base of the skull, and the use of the water attenuation correction factor (ACF or μ-value) for brain tissue (0.096 cm^{-1} instead of 0.099 cm^{-1} [11], [12]). These inaccuracies in the μ-maps will lead to incorrect quantification in the PET emission images. Such a bias was reported for the cerebellum, pons and brain stem by several HRRT users as documented in May 2007 by Koeppe [13], suspecting scatter or attenuation correction to be the source of the bias (12% lower pons/global mean ratios for the HRRT as compared to all other scanners included in the project). The suspicion was later directed at the attenuation correction alone through discussion and investigations amongst HRRT users, but with potential problems with using MAP-TR in scatter correction as documented in [10]. Quantitatively correct images are essential, especially when used for research purposes, e.g. in neuroreceptor imaging with quantification of binding potentials.

The objective of our work as presented in this paper was to improve the quantification of HRRT emission images by providing better μ-maps than what was available in the standard HRRT software. Thus we developed the transmission processing with total variation (TXTV) method. Its evolution is two-fold: Firstly, it introduces the use of scatter correction in the iterative reconstruction of the transmission image, and

S. H. Keller is with the Department of Clinical Physiology, Nuclear Medicine and PET, Rigshospitalet, Copenhagen University Hospital, Copenhagen, Denmark (sune@pet.rh.dk).

C. Svarer is with the Neurobiology Research Unit, Rigshospitalet, Copenhagen University Hospital, Copenhagen, Denmark (csvarer@nru.dk).

M. Sibomana was with the Department of Clinical Physiology, Nuclear Medicine and PET, Rigshospitalet, Copenhagen University Hospital, Copenhagen, Denmark. He is now with Sibomana Consulting, Emines, Belgium (sibomana@gmail.com).

secondly, it avoids segmentation errors using a simple threshold in combination with nonlinear total variation (TV) μ-map filtering.

We validated TXTV against μ-maps derived from CT scans, which can be considered as the gold standard for attenuation correction in PET (as it is in recent development of a MR-based attenuation correction for combined PET/MR scanners [14]). We also compared images acquired using the HRRT scanner to GE Advance PET scanner images which has been used widely in clinical research and daily clinical routine.

The TXTV method was released as part of the HRRT Users Community Software in January 2009 and is available to all HRRT users. The TXTV method has been described shortly in [15].

In the following we will describe the HRRT scanner and transmission processing methods, then evaluate the performance of TXTV using phantom and clinical human brain scans and finish with a discussion of the properties of this new and improved method.

II. Material and Methods

A. The HRRT Scanner, Transmission Scanning and Image Reconstruction

To achieve the highest possible resolution for human brain studies, the HRRT scanner [1], [2] has 119,808 crystals each 2.44x2.44 mm^2 in size, which is a less than half the crystal size of typical PET/CT scanners. They are arranged in two layers, in front 10 mm LSO and in back 10 mm LYSO, all organized in 8x8 detector blocks. Instead of the typical ring design the scanner contains 8 octagonally placed planar heads containing 9x13 of the before mentioned detector blocks. The scanner has a field of view (FOV) with an axial length of 252 mm and a diameter of 312 mm.

Transmission scans on the HRRT are performed using a ^{137}Cs point source with an energy of 662 keV, which is moved continuously in the axial direction and incrementally rotated in small steps (2 crystals by default) to cover an arc of 280°. The point source is collimated to irradiate only a few crystals opposite to the source. To account for emission contamination of the transmission signal when the tracer is injected prior to transmission scan, a virtual source measurement is done simultaneously to the transmission scan [8]. Typical transmission scans are performed with the source moving 50% of maximum axial speed resulting in a scan time of 6 min. Blank scans, which are not subject to acquisition time constraints, are performed at 10% of max axial speed (approx. 26 min scan time) to obtain high statistics datasets for normalization in the transmission image reconstruction. These are the default settings for the scanner as are the TX image size of 128 x 128 x 207 voxels (2.44 x 2.44 x 1.22 mm^3).

Emission (EM) images are reconstructed with a fast implementation of the 3-dimensional ordinary Poisson ordered subset expectation maximization (OP-OSEM3D) algorithm [16] including resolution modeling [17], [18], attenuation correction and scatter correction (16 subset, 10 iterations). The EM image matrix size is 256x256x207. The μ-maps have half the resolution in the transaxial planes but due to their low count statistics it makes no sense doubling it.

B. Patients and Scans

Two groups of patients were included in this study, recruited from ongoing clinical studies that were approved by the Ethics Committee of Copenhagen, Denmark and was in accordance with the Helsinki II declaration. The 4 volunteers in the first group were each injected with [^{18}F]-Fluorodeoxyglucose (FDG), a tracer with a high uptake in cells with high metabolism, e.g. in tumors and cortical brain cells. Figure 1A-B illustrates the latter. After 40-60 min at rest a 6 min transmission scan was performed followed immediately by a 40 min emission scan. The 4 subjects also had CT scans performed at a Siemens Biograph True-Point PET/CT as well as T1 weighted MR scans done on a Siemens 3T Trio, both acquired as part of the clinical research project they were participating in.

The second group included 5 normal healthy volunteers from a study using a bolus-infusion scheme to obtain steady-state conditions in the brain [19]. The tracer [^{18}F]-Altanserin was used to image the 5-HT2A receptor distribution in the brain (illustrated in Fig. 1C-E). The subjects were scanned twice while constant infusion of tracer was continued, first either at the Advance scanner (3 subjects) or at the HRRT scanner (2 subjects). The second scan was performed immediately after the first scan finished at the other scanner. Each scan was performed as 5 x 8 min frames but in a few cases the latter of the two scans were performed using 6 min frames or limited to 4 frames due to limited availability of tracer or subjects not being able to stay in the scanner for a full 40 min scan. All 5 subjects had structural high resolution T1 MR scans acquired at a Siemens Trio MR scanner (1x1x1 mm voxels). Scans were quantified as $BP_p=(C_{vox}-C_{ref})/C_p$ with cerebellum used as reference region and C_p measured from blood plasma samples corrected for metabolites (further details given later in the Validation section below).

For each subject the PET data (either FDG or Altanserin) were aligned with the high resolution structural T1 weighted MR image using the co-registration techniques with a mutual-information cost-function in SPM5 (http://www.fil.ion.ucl.ac.uk/spm/). All alignments have afterwards been carefully inspected visually and in some cases, the Advance Altanserin scans needed some additional manual correction of the rotation around the x-axis while none of the HRRT scans showed any need of manual adjustments.

C. Standard Method: MAP-TR

The recommended HRRT transmission processing method, MAP-TR [6], [7], [8], histograms the reconstructed μ-map to find peaks (assuming that most pixels are water/soft tissue) and applies a global scaling factor to all pixels to get the peak pixel values to fit the water μ -value at 511KeV (0.096 cm^{-1}). The scaling is used to correct for both the energy difference and scatter. Segmentation and thresholding are done as a part of the iterative reconstruction and the human brain prior has a four-modal distribution, with peaks at (centroid, sigma):

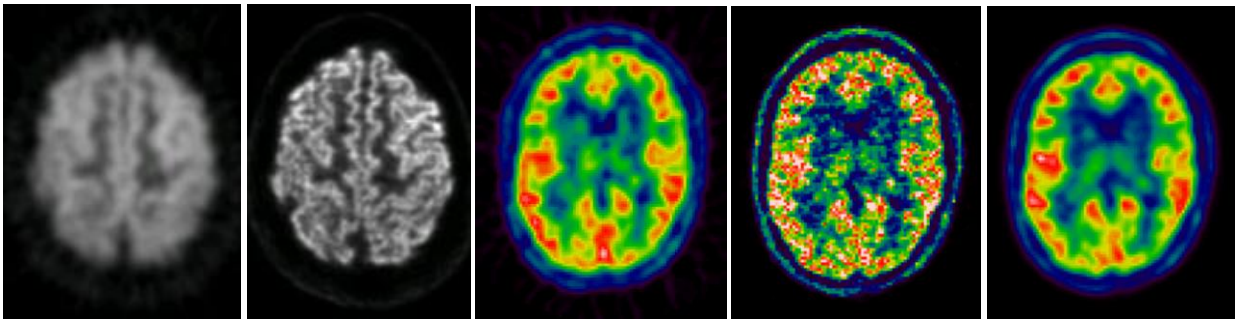

(a) (b) (c) (d) (e)

Fig 1. Examples of PET images from the HRRT and Advance scanners. The FDG scans from the Advance (**A**) and the HRRT (**B**) clearly illustrating the superior resolution of the HRRT. The Altanserin scans (distribution of the 5HT-2A serotonin receptors) are from the Advance (**C**) and the HRRT; unfiltered in (**D**) and filtered with a 6 mm Gaussian (FWHM 6x6x6 mm^3) in (**E**) for direct comparison to (**C**) at the resolution of the Advance.

0.000, 0.005 cm^{-1} (air); 0.030, 10.00 cm^{-1} (pixels located at the edge of the object, i.e. to allow for partial volume effects); 0.096, 0.020 cm^{-1} (soft tissue) and 0.110, 10.0 cm^{-1} (for bone). Thresholds between tissue classes are set to 0.030, 0.070 and 0.105 cm^{-1}.

D. New Method: TXTV

The TXTV method for transmission scan processing introduces scatter correction in the μ-map (image) reconstruction using the same iterative scheme as in MAP-TR including global scaling. Once the noisy initial image (see example in Fig. 4A) is done, we correct underestimated soft tissue voxels in a partial thresholding before doing a total variation filtering. These three steps will be described in the following.

1) Scatter Correction

The old (MAP-TR) equation to find the attenuation correction factor (ACF or μ-value) in the iterative reconstruction of the μ-map is $ln(ACF) = ln(bl/tx)$ where *tx* is the transmission scan and *bl* is a blank scan.

We have implemented the scatter correction developed for the ECAT ART scanner [20], where the assumption of the correction is to stretch the attenuation path length with a fraction that is independent of the object. The standard equation of the attenuation length to estimate the attenuation from blank and transmission scans, $ln(ACF) = ln(bl/tx)$, is modified in [20] to a first order function of $ln(bl/tx)$

$$\ln(ACF) = a + b * \ln\left(\frac{bl}{tx}\right)$$

where *a* and *b* are constants that we estimated experimentally using uniform phantoms with known μ-values (water and ^{68}Ge-epoxy). By adjusting the constants we obtained the expected μ -values across the phantoms and corrected for scatter without having to resort to segmentation and global scaling to fit the water μ-value at 511 keV as with MAP-TR. An absolute and fixed global scaling factor 1.116 (= 0.096 cm-1 / 0.086 cm-1) was, however, applied to get the μ-values at 511 keV from the ones measured at 662 keV, the energy of the ^{137}Cs HRRT transmission source. The factor is the ratio between the μ-values of water at 511 and 662 keV respectively, and this ratio is almost constant for other biological materials [21].

When we implemented this simple linear model, we were aware of the development of a more advanced scatter correction method for transmission data [22] on a small animal PET scanner, which could be adapted and implemented on the HRRT. We chose to implement the simpler linear method first and to try the advanced method if the results were not satisfactory, which was not the case.

2) Thresholding

The thresholding done in TXTV is not a traditional full dynamic range segmentation as in MAP-TR, it is a partial thresholding. The unprocessed (only reconstructed) HRRT μ-maps are noisy and contain underestimated pixels at the center of the brain due to residual scatter even though the scatter correction we have introduced reduces this effect). Our partial segmentation/thresholding process raises underestimated soft tissue pixels in the range [0.07, 0.099] to the brain tissue μ-map value of 0.099. After this step the μ-maps are still very noisy and needs filtering.

The overestimation of the skull seen with MAP-TR due to segmentation errors is avoided in TXTV as we: a) do not do any segmentation or thresholding in the range of bone (no segmentation above 0.099) and b) remove any peaks left in this range overestimating bone in the following step of nonlinear filtering described below (this range is still noisy and unprocessed from the raw reconstruction).

3) Nonlinear Filtering

The classic choice in molecular imaging would be to use Gaussian smoothing, but to preserve the finer bone segments at the base of the skull and get fairly sharp edges, we have chosen to use nonlinear total variation (TV) regularization [23]. Nonlinear filtering is normally considered slow, but using the settings we found to be optimal for TXTV in our work, μ-maps (image volume size 128 x 128 x 207) were filtered in less than three seconds on a standard laptop, which is an insignificant addition to the overall transmission processing time of 30 sec. on a typical reconstruction computer.

Total variation preserves structures and edges/boundaries in images while still removing noise, and the filtering (regularization) is optimized using an iterative solver. If one iterates TV regularization too far (starting from a noise-free photographic-like image) the result will often be a cartoon-like

image with flat plateaus separated by sharp edges, which is also the desired look of a well-segmented μ-map. Modeling the regularization as an energy minimization problem, TV can be formulated as

$$E(u) = \int_\Omega (u - u_0)^2 dx + \lambda \int_\Omega \psi(|\nabla_3 u|) dx$$

where u_0 is the input image and u the regularized output. Ω is the domain of our μ-map, x denotes the position in the image, λ is the weight controlling the degree of smoothing and ∇_3 is the 3D local spatial gradient operator. Since the function $|\cdot|$ is not differentiable at the origin, we replace it by the approximation $\psi(x) = \sqrt{x^2 + \varepsilon^2}$ with ε = 0.01 in this study. The second term of the energy is the TV smoothing or model term (the prior in a Bayesian MAP formulation of the problem), which would become Gaussian if the gradient was squared. The first term is a reaction or data term (the likelihood in a Bayesian formulation), which controls the degree of smoothing relative to the input image (through λ). By using calculus of variation we obtain the Euler-Lagrange equation

$$\frac{\partial E(u)}{\partial u} = (u - u_0) - \lambda \mathrm{div}_3 \left(\frac{\nabla_3 u}{\psi(|\nabla_3 u|^2)} \right) = 0$$

where div_3 is the 3D divergence operator and λ has been divided by 2. This nonlinear equation is solved using a fixed point scheme: The nonlinear parts are updated a number of times (outer iterations). After each update they are fixed while a linear Gauss-Seidel solver is used at the nonlinear system. The new value of each pixel (u_c) is found from Eq. (1) with the A's being the nonlinear parts that are kept constant during the inner iterations. The indexes in (1) denotes the compass directions **w**est, **e**ast, **n**orth and **s**outh, and **c**enter, **b**efore and **a**fter in the discrete image grid with a step size of 1 voxel, e.g. $u_w = u(x-1, y, z)$.

The nonlinear parts (the A's) are only updated in the outer iterations. They are directional symmetric, and from the example of A-west given in Eq. (2) the remaining 5 A's are easily found. For in-depth theory and a more exhaustive derivation of the final implementation in (1) and (2) we refer to [24]. C++ source code is available in the HRRT Users Software.

In our work to optimize the setting of TXTV, we ended up using 2 outer and 3 inner iterations with λ = 0.5 (and ε = 0.01), which are also the default (but not fixed) settings for TXTV in the HRRT Users Software. It was carefully confirmed visually on μ-maps, emission images and image arithmetic derivatives thereof, that further iterations did not improve the result. With a processing time of three seconds, the use of a convergence threshold to save time was never needed. Changing λ from 0.5 only slowed the convergence rate (lower λ) or resulted in clearly incorrect solutions due to over-regularization of the method (higher λ).

E. Validation

1) Comparison to CT-based μ-maps

For the 4 patients with ^{18}F FDG emission scans on the HRRT and CT scans, we obtained CT-derived μ-maps by backward-projection of the attenuation correction factors sinogram stored by the PET/CT system into image space (CT μ-map).

The algorithm used by Siemens in their PET/CT scanners to get from Hounsfield units at an effective CT energy of 80–140 keV to 511 keV of PET is described in [25] but parameters on the Siemens scanner used in this study are different than those given in the paper: At the 120 keV of our CT scans the break point on the scanner is 1070 (HU + 1000) while it was 1047 in the paper, and the slope below the break point is down from $9.6 \cdot 10^{-5}$ cm^{-1} to $9.5 \cdot 10^{-5}$ cm^{-1}. Otherwise, the parameters are as described in [25]. The CT-based μ-maps were registered to the HRRT μ-maps using Vinci 2.50 (Max-Planck Institut für Neurologische Forschung, http://www.nf.mpg.de/vinci/index2.html). The axial FOV of the CT images was smaller than HRRT FOV so the missing pixels in the registered CT μ-maps were replaced by HRRT TXTV μ-map values (Fig. 3D). For each subject, three emission images where reconstructed using a) the "gold standard" CT-based μ-map, b) the TXTV μ-map and c) the MAP-TR μ-map.

A probability based automatic delineation of volumes of interest [26] was used to delineate 45 volumes of interest (VOI) on MR images for each subject, which were registered to the HRRT emission images. The activity mean in each of the VOIs in the EM reconstructions were then compared: CT μ-map vs. MAP-TR μ-map and CT μ-map vs. TXTV μ-map. The VOIs are distributed throughout the brain and 35 of them are illustrated in [26].

$$u_c = \frac{\lambda(A_w \cdot u_w + A_e \cdot u_e + A_n \cdot u_n + A_s \cdot u_s + A_a \cdot u_a + A_b \cdot u_b) + u_{0,c}}{\lambda(A_w + A_e + A_n + A_s + A_a + A_b) + 1} \quad (1)$$

$$A_w \approx \frac{1}{\sqrt{(u_w - u_c)^2 + \frac{1}{16}(u_n - u_s + u_{nw} - u_{sw})^2 + \frac{1}{16}(u_a - u_b + u_{aw} - u_{bw})^2 + \varepsilon^2}} \quad (2)$$

2) HRRT vs. Advance

Advance scans where reconstructed using the GE standard filtered back-projection algorithm with a 6 mm FWHM Hanning filter. The HRRT scans were reconstructed using TXTV for attenuation correction and filtered after reconstruction with a 6 mm FWHM Gaussian to match the HRRT images to the lower Advance scanner resolution (see Fig. 1C-E). Individual frames of the 5x8min reconstruction (both scanners) where aligned using the reconcile principle from the AIR software package [27] if more than 2 mm motion was detected between any frames. As in the validation vs. CT, MR images were used for automatic delineation of VOIs and mean regional values for the neocortical, subcortical and cerebellar regions were extracted from the PET images. Further, the neo- and subcortical (C_{roi}) concentrations minus cerebellar (C_{ref}) concentration were calculated. The binding potential relative to plasma, BP_P, is proportional to this as the plasma concentration, C_P, is kept constant during both scans. It can be calculated as: $BP_p = (C_{roi} - C_{ref})/C_P$.

Similar to the HRRT, the Advance scanner uses rotating rod sources to do transmission scans for attenuation correction. But it uses two ^{68}Ge sources that emit photon pairs at 511keV such that no mapping in energy is needed. To our knowledge no bias in PET (brain) imaging on the Advance scanner has been reported and we have ourselves used it for more than 15 years without experiencing such problems.

F. Evaluation

1) HRRT Users Community Survey

TXTV was released as part of the HRRT Users Software in early 2009. We conducted a survey on the HRRT Users mailing list in Aug. 2012 to get an overview of the use of TXTV among the 17 HRRT centers. The questions asked in the mail were: "A) Do you use TXTV at all? B) How long have you (approximately) been using it? C) Do you use it for all human subject scans? D) Do you use it for animal scans? E) A rough number of how many scans you have used it for if possible. + Any comments on its use."

III. Results

A. Scatter Correction Parameters from Phantom Scans

The new HRRT μ-map reconstruction with scatter correction (reconstruction only, no thresholding or TV filtering) was used on two high statistics transmission scans (speed = 10, step = 2, 25 min) of a 20 cm cylinder phantom filled with water and the HRRT QC phantom; a 20 cm cylinder phantom filled with ^{68}Ge epoxy, both shown in Fig. 2. The μ-maps were uniform and the average value with absolute scaling was respectively 0.096 and 0.103 as expected at 511 keV. Two smaller water phantoms (D = 10 cm and D = 2 cm) were also scanned with the same settings and used to adjust the scatter correction parameters by computing the ratio between a central ROI (D = 8 cm) and an annulus (inner D = 16 cm, outer D = 18 cm) on the 20 cm phantoms. The parameter *a* was used to adjust the shape of the radial profile, whereas *b* was used to adjust the ROI average to the expected value and finally set to *b* = 1.18. Setting *a* = -0.14 gave an excellent ratio between the center ROI and the annulus (1.0 for the 20 cm water phantom and 0.99 for the germanium phantom). However, *a* = -0.1 gave a better agreement between

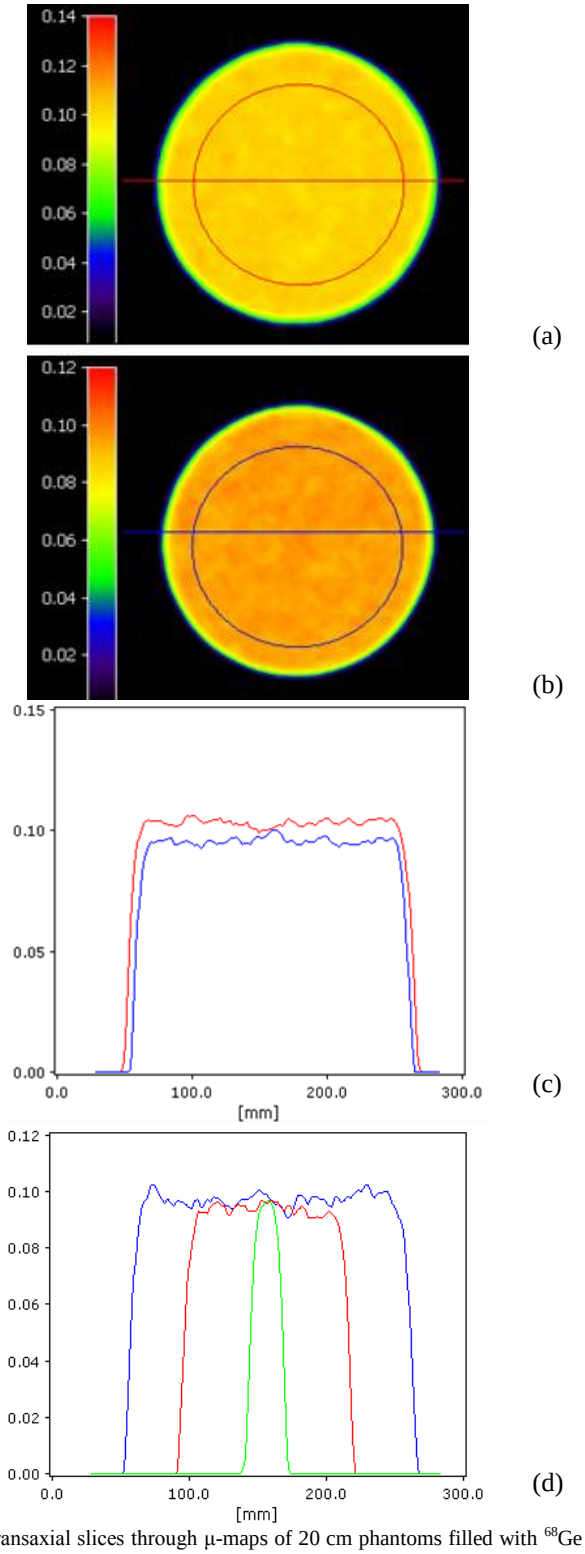

Fig. 2. Transaxial slices through μ-maps of 20 cm phantoms filled with ^{68}Ge epoxy (**A**) or water (**B**) and a plot (**C**) of the horizontal profiles through the phantoms (unfiltered) illustrating the high uniformity of the μ-maps. The red profile in (**C**) is across the ^{68}Ge epoxy phantom and the blue profile is across the water phantom (both shown as overlay in (**A**) and (**B**)). (**D**) shows a plot of similar horizontal profiles through the 3 water phantoms (2 cm in green, 10 cm in red and 20 cm in blue).

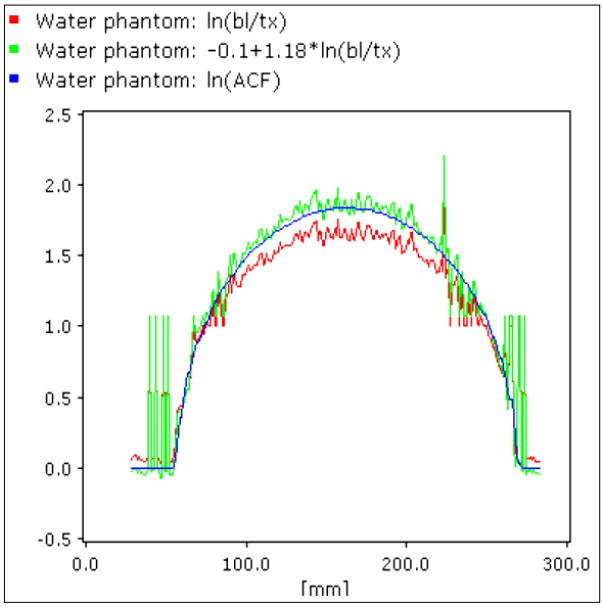

(a)

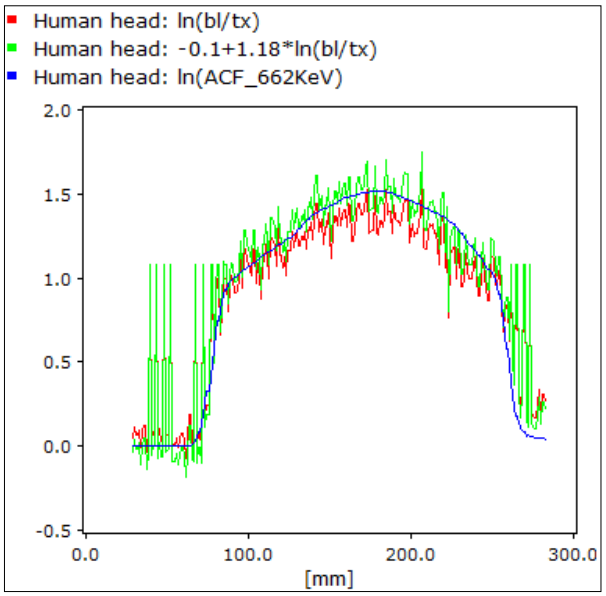

(b)

Fig. 3. (**A**) Radial profiles in the sinograms of the high statistics speed 10 transmission scan of the 20 cm water phantom. The correct ACF (blue) is a forward projection of the segmented μ-map (μ = 0.086 for water at 662 keV) and it is seen how the first order linear modeling for scatter correction (green) gets very close to the correct value compared to the standard method without scatter correction (red) which is about 10% off at the center. (**B**) Radial profiles in the sinograms of a human head scan at the normal speed 50 transmission scan with lower counts and thus higher noise than in (**A**). In (**B**) the blue ideal ACFs are projected from a CT-derived μ-map for the human head and scaled (0.086/0.096) to 662 keV. Again the first order linear modeling for scatter corrected profile in green is closer to the truth than the uncorrected profile in red, but does not work as well centrally as on the cylinder phantom, which is why we need to do a thresholding of the brain voxels to 0.099.

the three water phantoms for their profiles as shown in Fig. 2D, and the ratios were 0.977 for the 20cm water phantom and 0.973 for the germanium phantom.

In Fig. 3 profiles through the transmission sinograms of the 20 cm water phantom are shown. The correct *ln*(*ACF*) values are plotted in blue and the measured *ln*(*bl*/*tx*) value in red is a bit from the correct value (approx. 10% too low in images at 662keV). This is remedied with segmentation and global scaling in MAP-TR but tuning *b* to push the center peak in the sinogram profiles up to match the blue correct values curve (following the illustration in Fig. 3) and *a* to keep the tails down in place doing transmission scatter correction as for the ECAT ART in [20] we get the green curve, which is almost perfect (a bit too high, since *a* is not set to the ideal -0.14, but to the tradeoff value of -0.1). Fig. 3a and 3b show that the correction doesn't work as well for human as on cylindrical phantom, which explains the residual scatter and the need of a thresholding step. The difference between phantom and human head scans is due to two things: a) the more complex composition and shape of a human head; and b) the transmission scans speeds used (10 and 50). Due to radioactive dose and time constraints, human head scans should not be done at a lower speed

We have used the settings (*a*, *b*) = (-0.1, 1.18) in the remainder of this work and as default in the HRRT Users Software as the give the optimal balance between having flat profiles across the 20 cm phantoms (uniformity) and very similar results (ACFs) for different sized cylinder water phantoms.

B. Human Brain μ-maps

μ-maps for one of the four subjects who had FDG and CT scans are shown in Fig. 4. The CT-based μ-map (bottom right) is considered gold standard. Running TXTV on the scatter corrected μ-map (top left) result in a μ-map (bottom left) which is close to the "gold standard" CT μ-map, and in comparison to the standard HRRT MAP-TR μ-map (top right), more of the bone structures at the base of the skull are included. The skull in the MAP-TR μ-map is too thick compared to CT (and TXTV) as it is also known from literature [9]. The profiles through the μ-maps plotted in Fig. 5 shows how MAP-TR overestimates the values centrally in the skull and cuts off too steeply at the edge towards the brain as compared to CT.

The profiles in Fig. 5 also illustrates how TXTV has slightly varying brain tissue values but with less local variation than CT. MAP-TR has a completely flat profile through the brain where the values are also set too low to the water μ-value 0.096 cm^{-1} instead of the brain tissue μ-value 0.099 cm^{-1}.

C. Comparing CT-based, MAP-TR and TXTV μ-maps on FDG Images

To evaluate the bias in the two HRRT transmission processing methods, the old MAP-TR and the new TXTV, we compared the mean activities in 45 VOIs in the FDG PET emission images (EM) for each of the 4 subjects using different μ-maps: MAP-TR vs. CT-based and TXTV vs. CT-based. We computed the values 1 – [mean($EM_{\mu\text{-}HRRT}$)/mean($EM_{\mu\text{-}CT}$)] for all 45 VOIs where μ-HRRT is either MAP-TR or TXTV. The results are plotted in Fig. 6 and for each subject we calculated the mean and standard deviation

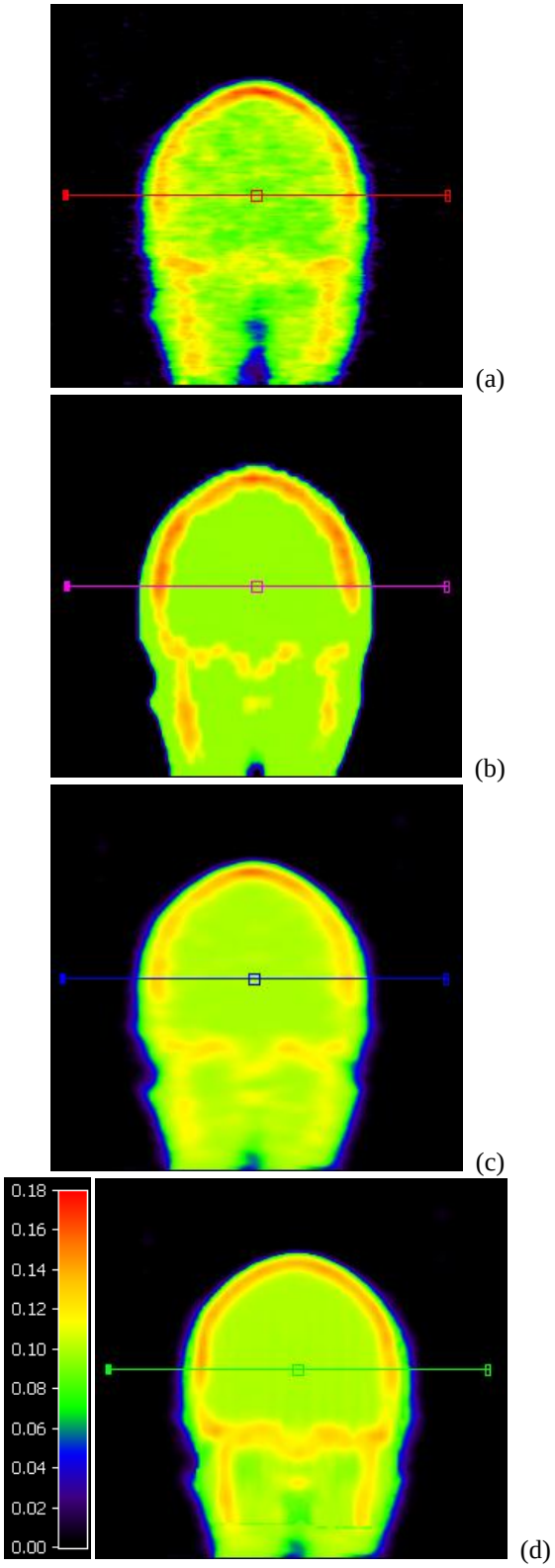

Fig. 4. Coronal view of human brain μ-maps (Subject 4): Reconstructed with scatter correction (**A**), MAP-TR (**B**), TXTV (**C**) and "gold standard" CT-based (**D**). A plot of the overlaid horizontal profiles is given in Fig. 5.

over the 45 VOIs for each of the two comparative measures and listed them in Table 1.

Inspecting the plots in Fig. 6 one sees that the ratio of EM means with HRRT μ-map over EM means with CT μ-map is

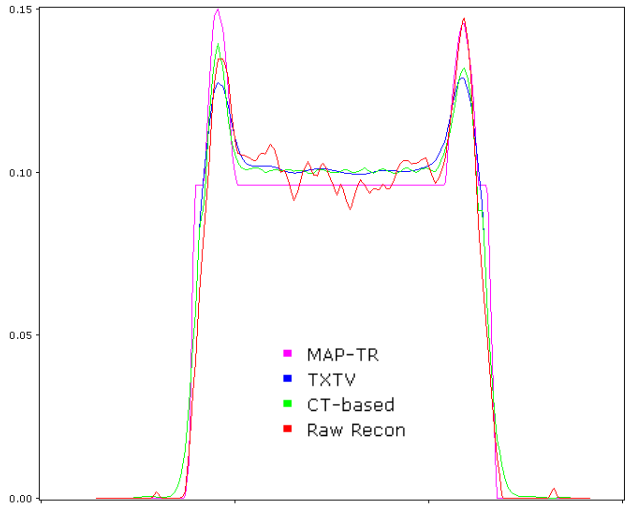

Fig. 5. Plot of the four profiles through the human brain μ-maps shown in Fig. 4.

TABLE 1
MEAN AND SD OF THE MEAN FDG UPTAKE IN THE 45 VOIS IN PERCENT

	Subject 1	Subject 2	Subject 3	Subject 4
MAP-TR vs. CT	-1.22±4.46	4.79±2.95	1.24±6.98	5.13±3.59
TXTV vs. CT	-0.71±2.43	1.13±2.06	0.24±2.22	1.27±1.65

notably larger with the old MAP-TR HRRT μ-map than with the new TXTV HRRT μ-map for all 4 subjects: Using TXTV μ-maps markedly lowers the error in the 45 VOIs as compared to using MAP-TR μ-maps.

For subjects 1-4 there are 15 + 22 + 24 + 25 = 86 of the 180 VOIs where MAP-TR is more than 5% different from the CT gold standard, while it is only 7 in total for TXTV (see Fig. 6). In subject 1 (positioned lower than the others) it is the Anterior Singulate, while it is the left and right Entorhinal Cortices for subjects 2, 3 and 4. These three regions are known to be noisy due to their small sizes and are not commonly reported in PET studies.

In Subject 1 we see little underestimation (only subject with negative mean values over all 45 VOIs in Table 1). Subject 1 was place very low in the scanner and thus very little of the neck was included in the FOV. When this happen less oblique angle LORs contribute to the voxels in the lower brain and thus errors in the μ-map from bad bone representation below the brain in MAP-TR is of less importance. We therefore mainly see the skull effect leading to brain voxel overestimation in Subject 1. The plots in Fig. 6 and the means in Table 1 for subjects 2 and 4 are dominated by underestimation as too little bone is segmented as bone below the brain for MAP-TR vs. CT and the mean for both changes substantially when switching to TXTV. Subject 3 is affected largely by both over- and underestimation yielding a small mean for MAP-TR and we only see a small improvement in the mean over the 45 VOIs (Table 1). Both the plots in Fig. 6 and the standard deviation for Subject 3 in Table 1 confirm the improvements when using TXTV (SD reduced by a factor of 3). A similar large drop in standard deviation with little change in the mean from MAP-TR vs. CT to TXTV vs. CT is

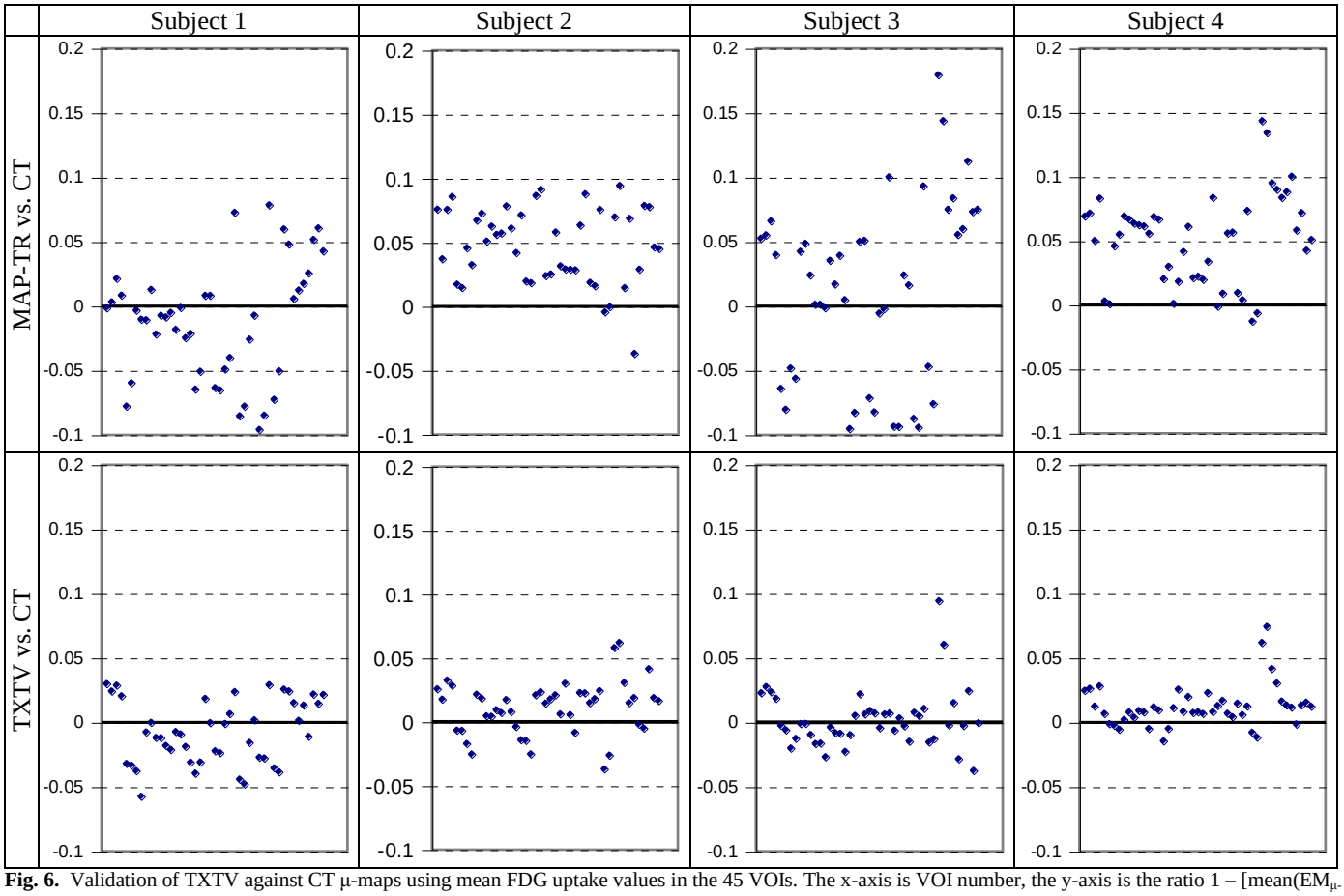

Fig. 6. Validation of TXTV against CT μ-maps using mean FDG uptake values in the 45 VOIs. The x-axis is VOI number, the y-axis is the ratio 1 – [mean($EM_{\mu\text{-HRRT}}$)/mean($EM_{\mu\text{-CT}}$)]. Top row: Old MAP-TR vs. CT. Bottom row: New TXTV vs. CT. Each column represents a subject. A positive value shows an underestimation relative to CT when using an HRRT μ-map (MAP-TR or TXTV) and a negative value is the sign of an overestimation.

seen for subject 1.

We performed a paired, two-tailed t-test on the MAP-TR and TXTV VOI mean FDG uptakes, mean($EM_{\mu\text{-HRRT}}$), which is same as doing the test on the differences mean($EM_{\mu\text{-HRRT}}$) - mean($EM_{\mu\text{-CT}}$). The resulting p-values for the 4 subjects are from subject 1 to 4: 0.0865, $8.32\cdot10^{-13}$, 0.552 and $1.28\cdot10^{-11}$. As expected TXTV is significantly different from MAP-TR for subjects 2 and 4 (p= 0.05), and it is of little surprise that TXTV is not statistically significant different from MAP-TR for subjects 1 and 3. This lack of significance does not change the fact that TXTV improves substantially over MAP-TR for all 4 subjects as shown by the plots in Fig. 6 and corresponding improvements in means and/or standard deviations (Table 1) for each subject.

Visual inspection of the PET images shows very small differences. Calculating difference images (per voxel $EM_{\mu\text{-HRRT}}/EM_{\mu\text{-CT}}$) as done for subject 4 in Fig. 7, clearly shows the quantitative differences. It is visually clear that using TXTV get you a lot closer to the CT gold standard than using MAP-TR does. Beside grave underestimation at the base of the brain as it was expected when using MAP-TR there is also severe overestimation in the brain regions close to where the skull is very thick and has too high ACF-values in MAP-TR μ-maps (compared to CT-based μ-maps). For TXTV the differences within the brain are small but some errors are seen outside the brain, and overall the correspondence between difference image inspection and VOI based analysis is high.

D. HRRT vs. Advance with Altanserin

Figure 8 shows the slope of the line C_{roi}-C_{ref} which is proportional to BP_P for constant C_P. For both the neocortical (C_{neo}-C_{ref}) and subcortical (C_{sub}-C_{ref}) regions the slope of the fitted line as a function of time for the five subjects is tested and found not significantly different from zero (one sample t-test, p=0.08 respectively p=0.10 for the two regions). This means that the last scan does not have significantly higher binding potential than the first scan. This suggests that we have achieved steady-state conditions during the two scans and that there is no significant difference in the quantitative results coming from the two scanners.

For Altanserin subjects 1, 2 and 3 we initially used MAP-TR for the HRRT data in our scanner comparison study but were not able to get matching slopes from the two scanners. As it turned out, getting matching slopes with TXTV was easy (see Fig. 8), and for the 2 patients scanned in the reverse order (HRRT first) we did not even compute results with MAP-TR as we had no reason to believe it would give results that quantitatively matched the Advance scanner (which we trusted to measure correctly).

E. HRRT Users Community Survey

We asked the 17 HRRT centers via the HRRT Users

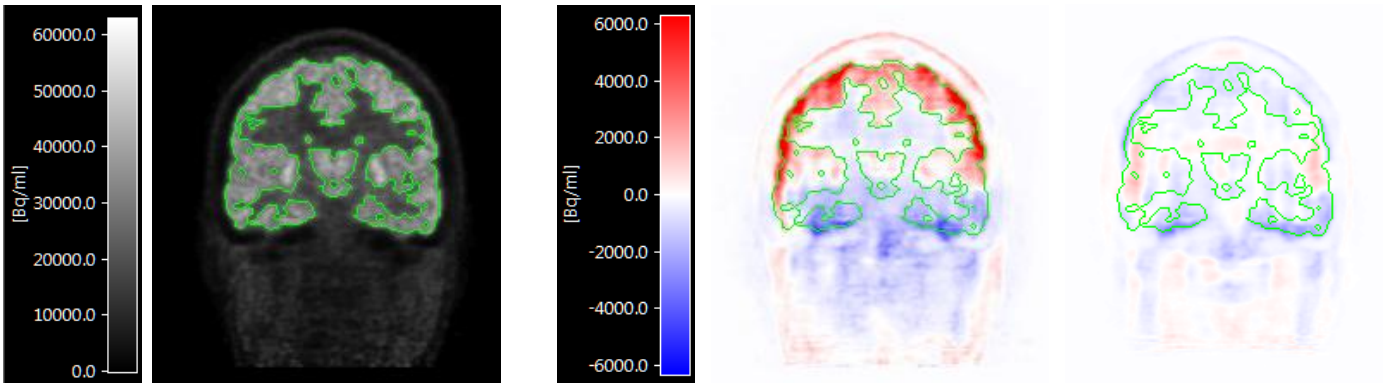

(a) (b) (c)

Fig. 7. Visual assessment of difference between using CT-based and HRRT μ-maps on FDG scans (subject 4). (**A**) FDG (EM) with a threshold contour, (**B**) $EM_{\mu\text{-}MAP\text{-}TR}$ - $EM_{\mu\text{-}CT}$ and (**C**) $EM_{\mu\text{-}TXTV}$ - $EM_{\mu\text{-}CT}$. The contour from **A** is overlaid on **B** and **C**. The scale for the subtraction images are set to ±10% of the maximum value in (**A**) and the images show that while TXTV still has some minor differences from CT-based attenuation correction, MAP-TR has more severe differences (confirming the general findings shown in Fig. 6).

mailing list to report their use of TXTV from its release in the HRRT Users Software in January 2009 until the time of the survey in August 2012. Eleven of the 17 centers replied, and of those 11 centers, 7 (64 %) are using TXTV. Two of the 4 not using it, wishes to do so. The 7 centers using it started to do so in 2009 (4) or 2010, and 2 have used it retrospectively on ongoing studies. All 7 centers are using it for all human scans and 2 also use it for animal studies. All in all it has been used on approximately 4500 scans by Aug. 2012. No issues on image quality and/or quantification when using TXTV have been reported.

IV. Discussion

We have shown on FDG data that using TXTV μ-maps for attenuation correction brings quantification of HRRT images closer to using CT-based μ-maps than the standard method of using MAP-TR μ-maps. MAP-TR has problems not only with segmentation of bones below the brain, resulting in underestimation in the lower brain, but also causes overestimation in the upper part of the brain near the skull as it assigns too high attenuation correction factor values to the skull. Both VOI analysis and visual inspection shows that the bias in the brain is minimized with TXTV.

Using a very stable bolus-infusion approach for injection of Altanserin, we have compared human brain images from the Advance scanner and the HRRT scanner, the latter reconstructed using TXTV μ-maps. Filtering the HRRT images to Advance scanner image resolution yields the same specific binding with the Advance and the HRRT both in the neo- and subcortical regions. It is therefore concluded that comparable results can be achieved when the HRRT scanner with TXTV is used for measuring binding in the brain.

Further, it is demonstrated that the HRRT images have a higher contrast between high and low binding areas in the brain than images acquired on a traditional clinical PET scanner, such as the Advance scanner.

Since TXTV was released to the HRRT Users in early 2009 it has been used to reconstruct more than 4000 scans, mostly scans of the human brain, with no reports of bias. For the animal scans reconstructed with the TXTV μ-maps, no validation have been made, but since animals scanned in the HRRT (pigs, smaller primates, rodents) have less bone mass than humans, no major issues are expected, although caution should be taken if introducing new fixation devices.

In [11] MAP-TR with the μ-value of brain tissue raised from 0.096 cm^{-1} to 0.0994 cm^{-1} was analyzed and even though it improved over standard MAP-TR, it also performed worse, e.g. in the central regions of the brain: Using a correct brain tissue μ-value with MAP-TR does not do the trick.

The improvements in TXTV are threefold: 1) The use of scatter correction in transmission scan reconstruction, 2) applying total variation filtering, and 3) changing the μ-value of brain/soft tissue from 0.096 cm^{-1} to 0.099 cm^{-1}. This have brought us very close to using CT-based μ-maps, but in attempt to see if we could lower the bias even more, we tried to extend the threshold process to also cover the range between brain tissue and bone and do additional morphological opening before the TV filtering, but all attempts resulted in the loss of the bone below the brain and gave higher bias (in the same range as the MAP-TR bias). Thus it seems we need to add additional information to further improve the HRRT μ-maps. One option is to use brain atlas modeling which should give a reasonable map of bones below the brain. It is, however, questionable if we would get closer to using CT-based μ-maps as the remaining bias with TXTV is within the range of noise expected when comparing PET images and thus hardly qualifies as a bias.

Many human brain scans on the HRRT are done as part of neurological research protocols which also includes MR scans for the subjects, but given the difficulties of segmenting bone in MR-based attenuation correction [14], [28] it is more likely that adding a transmission source to PET/MR scanners would help PET/MR attenuation correction than using MR would help HRRT attenuation correction.

The improvements from using TXTV do not come alone from improved attenuation correction in the reconstruction: The improved μ-map also benefits the scatter correction as it was shown in [10]. The scatter is scaled according to the signal outside the object being scanned, which is pure scatter (no material to give signal). The μ-map is used to mask the

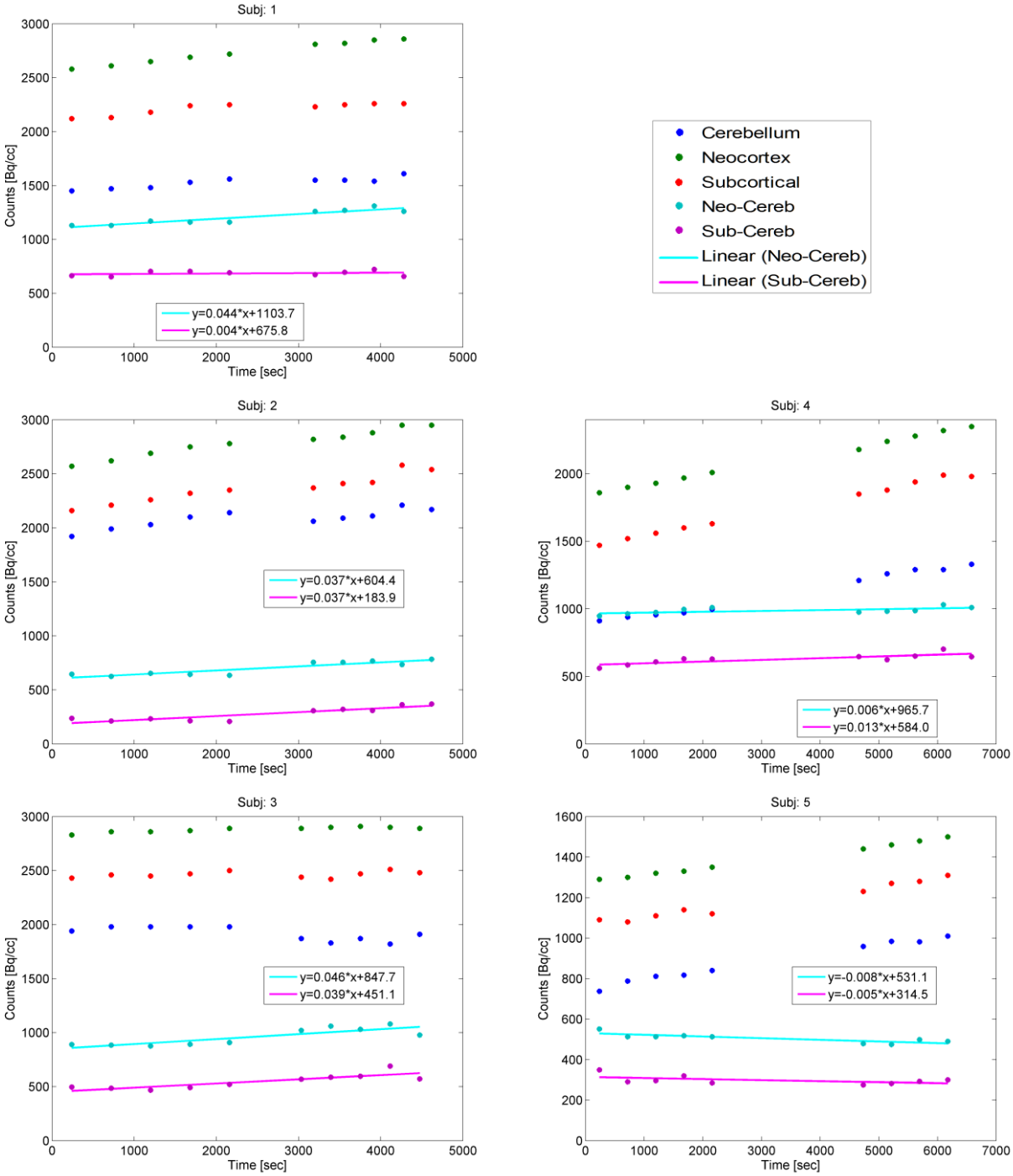

Fig. 8. Time activity curves from three brain regions (neo-, subcortical and cerebellum = non-specific binding) and the specifically bound activity (C_{roi}-C_{ref}) in the neo- and subcortical regions with linear fitting. The resolution in the HRRT image has been matched to the resolution in the Advance image using a 6x6x6 mm FWHM Gaussian spatial filter. Left column, subjects 1-3: Advance scan performed first. Right column, subjects 4-5: HRRT scan performed first. Data for latter scan were decay corrected to start time of the first performed scan.

object, and for tracers with high uptake in the skin or otherwise near the surface, small errors in the mask (badly segmented mask or common small subject motion) it can cause overestimation of scatter if material with uptake is considered background (= pure scatter). Due to the soft edges from TV filtering in TXTV, TXTV is more robust against this error than MAP-TR is as shown in [10].

Like the HRRT, the Advance scanner uses a transmission source to obtain μ-maps with no biases reported to date. We could scan longer with the existing source (higher dose, possible patient motion), but given the comparison we have done here, Advance vs. HRRT with TXTV (as well as comparison to CT); HRRT attenuation correction can most likely not be improved significantly for human brain scans.

V. Conclusion

The TXTV method for transmission scan reconstruction and

processing have been demonstrated to produce PET images which are quantitatively close to images reconstructed using the gold standard CT-based attenuation correction. Further, the TXTV reconstructed images are also close to GE Advance scanner images after degrading HRRT images to the Advance scanner resolution. We can therefore recommend the new TXTV method for reconstruction of PET scans of the human brain acquired at the HRRT scanner.

ACKNOWLEDGMENT

Thanks to the John and Birthe Meyer Foundation for graciously donating the HRRT scanner to Rigshospitalet. Parts of the work (Advance-HRRT comparison using Altanserin data) were funded by the EC - FP7-project Euripides, HEALTH-F5-2007-201380. Thanks to Søren Holm, Rigshospitalet, for providing insights on the Advance scanner and the intricate details of PET physics. Charles Watson and Christian Michel (Siemens, Knoxville, TN, USA) are thanked for their help and guidance in the adaption of the TX scatter correction method used for the ECAT ART.

REFERENCES

[1] K. Wienhard, M. Schmand, M. E. Casey, K. Baker, J. Bao *et al*., "The ECAT HRRT: performance and first clinical application of the new high resolution research tomography," *IEEE Trans. Nucl. Sci.*, vol. 49, pp. 104-10, 2002.

[2] H.W.A.M. de Jong, F.H.P. van Velden, R.W. Kloet, F.L. Buijs, R. Boellaard and A.A. Lammertsma, "Performance evaluation of the ECAT HRRT: an LSO-LYSO double layer high resolution, high sensitivity scanner," *Phys. Med. Biol.*, vol. 52, pp. 1505-26, 2007.

[3] V. Sossi, H. W. A. M. de Jong, W. C. Barker, P. Bloomfield, Z. Burbar, M.-L. Camborde, C. Comtat, L. A. Eriksson, S. Houle, D. Keator, C. Knob, R. Krais, A. A. Lammertsma, A. Rahmim, M. Sibomana, M. Teras, C. J. Thompson, R. Trebossen, J. Votaw, M. Walker, K. Wienhard, D. F. Wong, "The second generation HRRT - a multi-centre scanner performance investigation," *IEEE Nuclear Science Symp. Conf. Rec.*, vol. 4, pp. 2195-99, 2005.

[4] O. V. Olesen, M. Sibomana, S. H. Keller, F. Andersen, J. Jensen, S. Holm, C. Svarer and L. Højgaard, "Spatial resolution of the HRRT PET scanner using 3D-OSEM PSF reconstruction," *IEEE Nuclear Science Symp. Conf. Rec. (NSS/MIC)*, pp. 3789-90, 2009.

[5] B. W. Jakoby, Y. Bercier, M. Conti, M. E. Casey, B. Bendriem, D. W. Townsend, "Physical and clinical performance of the mCT time-of-flight PET/CT scanner," *Phys. Med. Biol.*, vol. 56, no. 8, pp. 2375-89, 2011.

[6] C. Knoess, J. Rist, C. Michel, Z. Burbar, L. Eriksson, V. Panin *et al*., "Evaluation of single photon transmission for the HRRT," *IEEE Nuclear Science Symp. Conf. Rec.*, vol. 3, pp. 1936-40, 2003.

[7] J. Nuyts, P. Dupont, S. Stroobants, A. Maes, L. Mortelmans, P. Suetens, "Evaluation of Maximum-Likelihood based attenuation correction in positron emission tomography," *IEEE Trans. Nucl. Sci.*, vol. 46, issue 4, pp. 1136-41, 1999.

[8] M. Sibomana, L. Byars, V. Panin, M. Lenox, F. Kehren *et al*., "Simultaneous measurement of transmission and emission contamination using a collimated ^{137}Cs point source for the HRRT," *IEEE Nuclear Science Symp. Conf. Rec.*, vol. 4, pp. 2647-51, 2004.

[9] F.H.P. van Velden, R.W. Kloet, B.N.M. van Berckel, C.F.M. Molthoff, H.W.A.M. de Jong, A.A. Lammertsma and R. Boellaard , "Impact of attenuation correction strategies on the quantification of High Resolution Research Tomograph PET studies," *Phys. Med. Biol.*, vol. 53, pp. 99-118, 2008.

[10] J. M. Anton-Rodriguez, M. Sibomana, M. D. Walker, M. C. Huisman, J. C. Matthews, M. Feldmann, S. H. Keller and M.-C. Asselin, "Investigation of motion induced errors in scatter correction for the HRRT brain scanner," *IEEE Nuclear Science Symp. Conf. Rec. (NSS/MIC)*, pp. 2935-40, 2010.

[11] Y. D. Son, H. K. Kim, S. T. Kim, N. B. Kim, Y. B. Kim, Z. H. Cho, "Analysis of biased PET images caused by inaccurate attenuation coefficients," *J. Nucl. Med*., vol. 51, no. 5, pp. 753-60, 2010.

[12] International Commission on Radiation Units and Measurements (ICRU), "Tissue Substitute in Radiation Dosimetry and Measurement," ICRU, Bethesda, MD, Report 44, 1989.

[13] R. Koeppe. (2007, May 8). *The Alzheimer's Disease Neuroimaging Initiative PET Core* [Online]. Available: http://www.loni.ucla.edu/twiki/bin/view/ADNI/ADNIPETCore

[14] M. Hofmann, I. Bezrukov, F. Mantlik, P. Aschoff, F. Steinke, T. Beyer, B. J. Pichler, B. Schölkopf, "MRI-based attenuation correction for whole-body PET/MRI: quantitative evaluation of segmentation- and atlas-based methods," *J. Nucl. Med.*, vol. 52, no. 9, pp. 1392-9, 2011.

[15] M. Sibomana, S. H. Keller, C. Svarer, O. V. Olesen, F. Andersen, S. Holm, L. Højgaard, "New attenuation correction for the HRRT using transmission scatter correction and total variation regularization," *IEEE Nuclear Science Symp. Conf. Rec. (NSS/MIC)*, pp. 3284-86, 2009.

[16] I. K. Hong, S. T. Chung, H. K. Kim, Y. B. Kim, Y. D. Son, Z. H. Cho, "Ultra fast symmetry and SIMD-based projection-backprojection (SSP) algorithm for 3-D PET image reconstruction," *IEEE Trans. Med. Imag*., vol. 26, pp. 789-803, 2007.

[17] C. Comtat, F. C. Sureau, M. Sibomana I. K. Hong, N. Sjöholm, R. Trébossen, "Image based resolution modeling for the HRRT OSEM reconstructions software," *IEEE Nuclear Science Symp. Conf. Rec.*, pp. 4120-23, 2008.

[18] F. C. Sureau, A. J. Reader, C. Comtat, C. Leroy, M. J. Ribeiro, I. Buvat, R. Trébossen, "Impact of image-space resolution modeling for studies with the high-resolution research tomography," *J. Nucl. Med.*, vol. 49, pp. 1000-8, 2008.

[19] L. H. Pinborg, K. H. Adams, C. Svarer, S. Holm, S. G. Hasselbalch, S. Haugbøl, J. Madsen and G. M. Knudsen, "Quantification of 5-HT2A receptors in the human brain using [18F]altanserin-PET and the bolus/infusion approach," *J. Cereb. Blood Flow Metab.*, vol. 23, no. 8, pp. 985-96, 2003.

[20] C. C. Watson, W. F. Jones, T. Brun, K. Baker, K. Vaigneur and J. Young, "Design and performance of a single photon transmission measurement for the ECAT ART," *IEEE Nuclear Science Symp.*, vol. 2, pp. 1366-70, 1997.

[21] S.K. Yu and C. Nahmias, "Single-photon transmission measurements in positron tomography using ^{137}Cs," *Phys. Med. Biol.*, vol. 40, pp. 1255-66, 1995.

[22] E. Vandervoort and V. Sossi, "An Analytical Scatter Correction for Singles-Mode Transmission Data in PET," *IEEE Trans. Med. Imag*., vol. 27, no. 3, pp. 402-412, 2008.

[23] L. Rudin, S. Osher and E. Fatemi, "Nonlinear total variation based noise removal algorithms," *Physica D*, vol. 60, pp. 259-68, 1992.

[24] S. H. Keller, "Video Upscaling Using Variational Methods," Ph.D. dissertation, Faculty of Science, University of Copenhagen, 2007. [Online]. Available: http://image.diku.dk/sunebio/Afh/SuneKeller.pdf

[25] J. P. Carney, D. W. Townsend, V. Rappoport, B. Bendriem, "Method for transforming CT images for attenuation correction in PET/CT imaging," Med. Phys., vol. 33, no. 4, pp. 976-83, 2006.

[26] C. Svarer, K. Madsen, S. G. Hasselbalch, L. H. Pinborg, S. Haugbøl, V. G. Frøkjaer, S. Holm, O. B. Paulson and G. M. Knudsen, "MR-based automatic delineation of volumes of interest in human brain PET images using probability maps," *Neuroimage*, vol. 24, no. 4, pp. 969-79, 2005.

[27] R. P. Woods, S. T. Grafton, C. J. Holmes, S. R. Cherry, J. C. Mazziotta, "Automated image registration: I. General methods and intrasubject, intramodality validation," *J. Comput. Assist. Tomogr.*, vol. 22, pp. 139-52, 1998.

[28] S. H. Keller, S. Holm, A. E. Hansen, B. Sattler, F. Andersen, T. L. Klausen, L. Højgaard, A. Kjær and T. Beyer, "Image artifacts from MR-based attenuation correction in clinical, whole-body PET/MRI," *Magn. Reson. Mater. Phy. (MAGMA)*, vol. 26, issue 1, pp. 173-81, 2013.